Out-of-Plane Nanoscale Reorganization of Lipid Molecules and Nanoparticles Revealed by Plasmonic Spectroscopy

Matthew R. Cheetham[1], Jack P. Griffiths[1], Bart de Nijs[1], George R. Heath[2], Stephen D. Evans[2], Jeremy J. Baumberg*[1] and Rohit Chikkaraddy*[1]

[1] NanoPhotonics Centre, Cavendish Laboratory, Department of Physics, JJ Thompson Avenue, University of Cambridge, Cambridge, CB3 0HE, United Kingdom

[2] School of Physics and Astronomy, Woodhouse Lane, University of Leeds, Leeds, LS2 9JT, United Kingdom

KEYWORDS: Single-molecule, Lipid bilayers, Plasmonics, Nanocavities, Nano-assembly, Purcell factor.

ABSTRACT.

Lipid bilayers assembled on solid substrates have been extensively studied with single-molecule resolution as the molecules diffuse in 2D, however the out-of-plane motion is typically ignored. Here we present sub-nanometer out-of-plane diffusion of nanoparticles attached to hybrid lipid bilayers (HBLs) assembled on metal surfaces. The nanoscale cavity formed between Au nanoparticle and Au film provides strongly-enhanced optical fields capable of locally probing HBLs assembled in the gaps. This allows us to spectroscopically resolve the nanoparticles assembled on bilayers, near edges, and in membrane defects, showing the strong influence of charged lipid rafts. Nanoparticles sitting on the edges of the HBL are observed to flip onto and off the bilayer, with flip energies of ~10 meV showing how thermal energies dynamically modify lipid arrangements around a nanoparticle. We further resolve the movement of individual lipid molecules by doping the HBL with low concentrations of Texas-red (TxR) dye-labeled lipids.

TOC Graphic

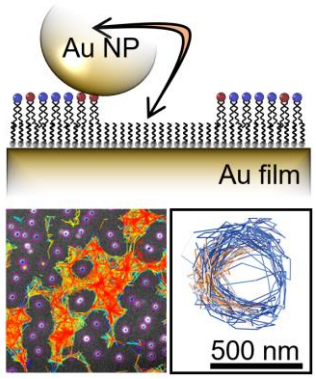

Lipid membranes are of vital importance for the function and survival of cells. Many of the processes in these membranes are understood only at a qualitative level, largely due to the small length- and fast time-scales involved. These systems are intrinsically fragile and environment specific, making them difficult to probe. The development of nanoscopic optical tools which minimally interfere with membrane function are thus in high demand[1,2]. Metal nanoparticles (NPs) are used to track and image diffusion of molecules and proteins within cell membranes, but the role of these NPs in modifying membrane dynamics remains unclear[3]. NPs either rupture through the cell membrane furnishing their use as therapeutic agents[4] as well as to induce cytotoxicity[5,6], or rest on the membrane giving imaging capabilities. These contradictory behaviors are linked to the different chemical and physical properties of NPs within membranes[7–9].

The complexity of lipid membrane diffusion has led to the 'fluid mosaic' model[10] being replaced with the 'picket fence' model[11], accounting for the very inhomogeneous nature of cell membranes with a great deal of compartmentalization and scaffolding. This gives rise to anomalous diffusion within the bilayer[17,19], which cells are believed to control in order to alter reaction pathways. Here we use hybrid lipid bilayers (HBLs) as model systems and study their interaction with AuNPs to develop tools to better understand the nanoscale inhomogeneity of HBLs[12,13] and the complex diffusion of NPs on such surfaces[14,15].

Advanced techniques to track nanoscale diffusion of lipids within a membrane currently rely on tagging lipids with dyes[16–18] or nanoparticles[13,15,19–22] and imaging using fluorescence or interferometric scattering respectively. These show in-plane (2D) diffusion of lipids with high spatial accuracy and time resolution, but ignore nanoscale out-of-plane motion due to insensitivity to displacements in this dimension <10 nm. Here we present nanoscale out-of-plane motion of lipid molecules in supported bilayers and their reorganization on interaction with metal NPs.

Nanostructures made of noble metals, such as the AuNPs used here, strongly confine light below the diffraction limit with minimal perturbation to the local environment. Their strong optical signatures make them ideal to probe cell membranes. Optically-excited collective oscillations of free electrons ('plasmons') on the metal confine optical fields tightly to a nanostructure[23,24]. This localized optical field enhances light-matter interactions, allowing single-molecule sensitivity using Purcell-enhanced fluorescence (PL), surface-enhanced Raman scattering (SERS), or absorption[1,25,26]. However, this enhancement requires assembly of metal nanostructures with narrow gaps or rod-like structures with large aspect ratios.

Here we construct nanoparticle-on-mirror (NPoM) cavities in which hybrid lipid bilayers (HBLs) are assembled between a flat gold surface and 100 nm diameter gold nanoparticles (AuNPs) (Fig. 1a,b), similar to previous reports[27]. The lipid molecules are assembled in a home-built flow-cell

system, which keeps the samples hydrated. The lower leaflet of the HBL consists of octadecanethiol (ODT) assembled onto the template-stripped gold substrate. The upper leaflet is formed by incubation of lipid vesicles containing POPC and a small amount of DOTAP (chemical structures Fig. 1c).

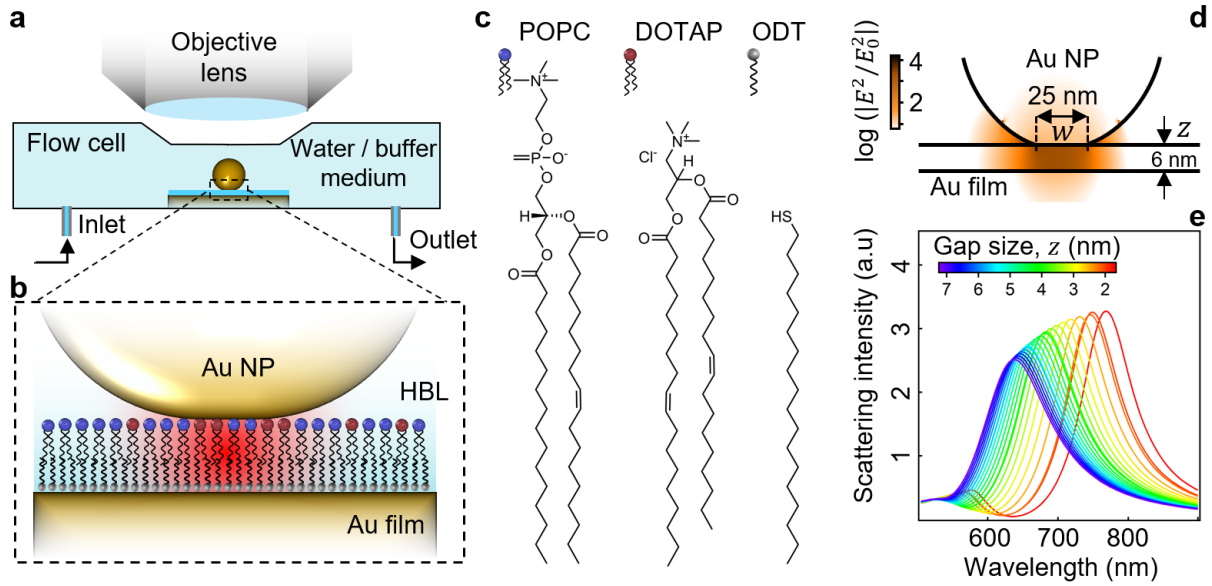

Figure 1. Experimental setup. (a) Schematic of flow-cell showing sealed NPoM sample underneath a ×100 long-working-distance 0.8NA objective. (b) Enlarged schematic of NPoM, showing hybrid bilayer in a plasmonic cavity formed between the AuNP and Au film. (c) Chemical structures of the bilayer constituents. (d) 3D FDTD simulation showing spatial distribution of enhanced plasmonic intensity. (e) Simulated scattering spectra from NPoMs with various gaps, used to calibrate darkfield resonance peak *vs* gap size.

The charge oscillations in each AuNP couple with image charges within the polarizable Au mirror underneath. This enhances the electromagnetic field intensity in the gap by four orders of magnitude (E^2/E_0^2) in an area of lipid molecules 30 × 30 nm^2 (Fig. 1d)[28,29], allowing direct optical access for PL and SERS. The wavelength of light resonantly trapped in the plasmonic gap is very sensitive to the separation of the nanoparticle from the metal surface, as seen from scattering spectra calculated with finite-difference time-domain (FDTD) simulations for various gap sizes (Fig. 1e), and experimentally confirmed using dark-field spectroscopy[27,30–32].

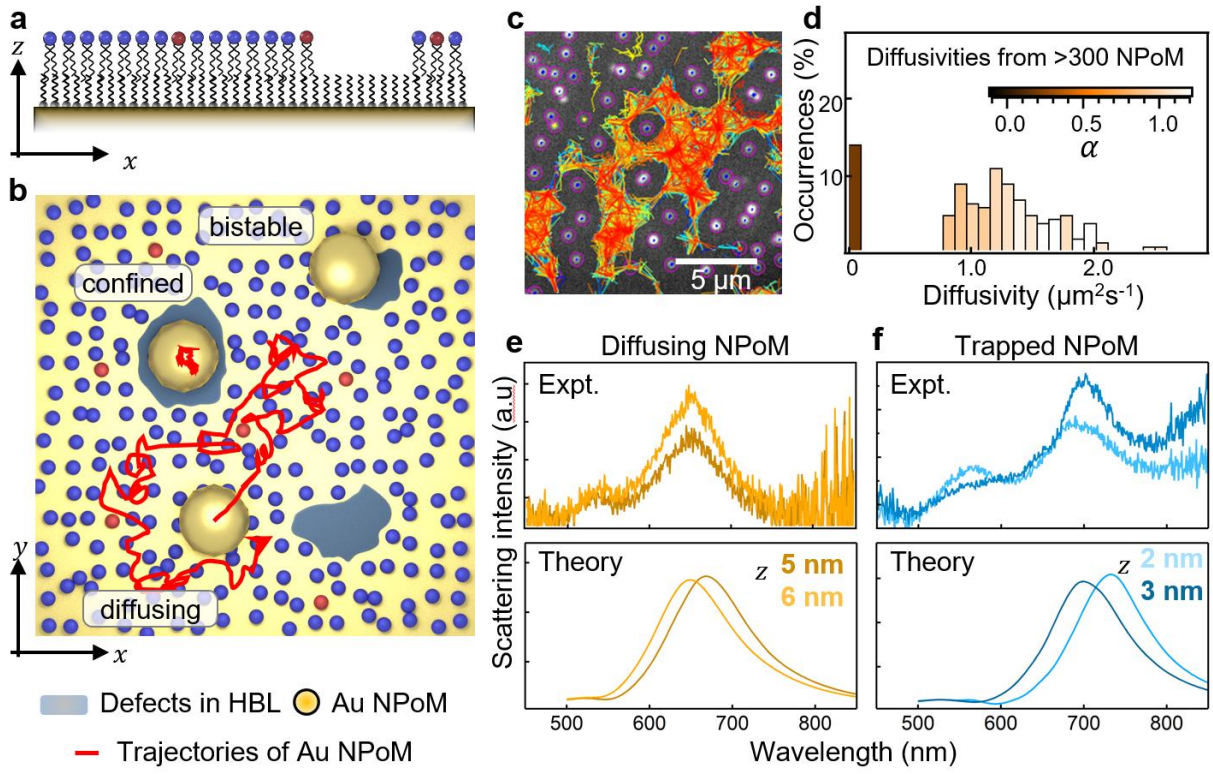

Figure 2. (a) Side-view of a hybrid bilayer with a defect. (b) Top-down schematic with defects and AuNPs, together with example diffusion trajectories (red tacks). (c) Example image from analyzed darkfield video showing AuNPs on the bilayer. Stuck AuNPs exhibit confined diffusion (purple circles). Trajectories of other AuNPs are tracked with the trajectory color indicating their diffusivities, and (d) show a histogram of diffusivities obtained from the filtered video (ignoring immobile AuNPs). The color scale depicts the average anomalous exponent α obtained from the particle trajectories (described in further detail below). (e,f) Experimental and theoretical darkfield spectra of (e) diffusive and (f) confined AuNPs at two different points in their trajectories *vs* gap sizes.

Dark-field videos of this self-assembled system at room temperature (Fig. 2) show three distinct types of events which help unravel the nanoscopic assembly and properties of the HBL: (i) 2D freely diffusing NPs, (ii) NPs trapped in nanoscopic wells, and (iii) blinking NPs. These events are shown schematically in Fig. 2a,b, each corresponding to a different local HBL environment around the corresponding NPoMs. The detected trajectories of NPs can be seen in Fig. 2c, and a histogram of diffusivities from these trajectories in Fig. 2d. The color scale here gives an indication of the average anomalous exponent (discussed in detail below) for each histogram bin. A large fraction of nanoparticles prefer to attach around defects in these bilayers, and thus appear immobile. Au nanoparticles landing on a completely intact bilayer however result in freely diffusing NPs by virtue of the fluidic nature of the upper HBL leaflet. The presence of the lipid layer is verified using force-distance measurements with AFM, which give the characteristic

'punch through' of the lipid layer (see all AFM images in Supporting Information Fig. S8). AFM also shows defects in the template stripped Au surface and preferential adsorption of AuNPs within these defects, however such weakly scattering NPs will not be captured in dark-field images.

These observations are complemented by detailed characterization of the dynamics using time-dependent dark-field spectra collected on individual NPoMs in the diffusing and trapped states. For NPoMs that are diffusing, the dark-field resonance is always observed to be at 650 nm (Fig. 2e). This corresponds to gap sizes z = 5-6 nm which agrees with the expected height of the HBL. However, for trapped NPoMs the resonance is further red-shifted to 750 nm (Fig. 2f) which corresponds to a gap size of 2 nm, the approximate thickness of the ODT monolayer.

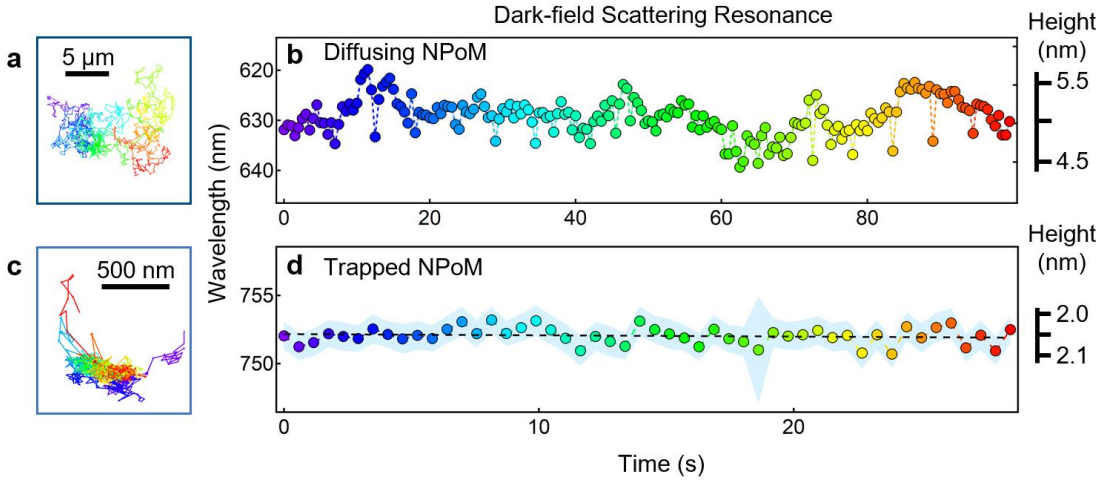

Figure 3. Tracking z-diffusion of the AuNPs on the lipid bilayer. In-plane (x, y) particle tracks (left) and dark-field resonant peak position as a function of time (right) of (a,b) mobile AuNP, and (c,d) confined AuNP. Peak positions are converted into z-separation using calibrated model (see text). Mobile AuNP shows height variations of ~0.5 nm, much larger than variations for the trapped particle.

To understand the diffusion of NPs on a HBL, the diffusion of many individual NPoMs are tracked. Many of the NPoMs are found to diffuse along micron lengths with typical diffusivity of 1.5 $\mu m^2 s^{-1}$ (Fig. 2d), similar to previous measurements using fluorescence imaging[33]. Correlating the dark-field videos (Supporting Information) with tracks from the 2D diffusion of individual NPoMs, we collect the spectroscopic signatures while nanoparticles diffuse laterally across the HBL (Fig. 3a). For improved signal-to-noise, the spectra are integrated over 500 ms compared to images acquired at 50 ms. The tracked dark-field resonance of a diffusing NPoM over time reveals z-motion of the AuNP height on the HBL (Fig. 3b), and time-resolved dark-field spectra of several more diffusing NPoMs are shown in the Supporting Information (Fig. S4). Changes in the resonance wavelength reveal out-of-plane motion of up to 1 nm, sub-nanoscopic motion which has been hypothesized[34,35] but never measured before.

The dark-field videos (Fig. 2c) show that the diffusing NPs are excluded from approaching trapped NPoMs closer than 3 μm, more than 30× larger than the NP size, repelling the diffusing NPs. Single particle tracking of all NPs in the recorded video (Fig. S2a-c, images with all tracks) shows this clearly from histograms of the spacing between nearest-neighbors (Fig. S3). Our observation is unexpected, since AFM confirms that the lipid layer is intact right up to the defect without displaying any topographical variation (Fig. S8). This implies that the 'exclusion zone' is likely electrostatic in nature and may be related to the recruitment of charged DOTAP lipids by the NP, creating a repulsive 'raft' in the lipid layer (a form of quasi-2D charge double layer). The NP diffusion rate is not significantly affected by the DOTAP concentration (Fig. S2d-f). However, the exclusion area strongly depends on [DOTAP], since the number of DOTAP molecules needed to stabilize the NP on the HBL remains fixed whilst the total number of available DOTAP molecules changes (Fig. S3d,e). The boundary of the exclusion zone appears sharp for larger DOTAP concentrations but more diffuse for lower concentrations. An additional observation is that more NPs diffuse freely in 2D on the membrane surface at higher [DOTAP], although the mean diffusivity of the diffusing NPs is not affected significantly. We also note that for 0% DOTAP, only immobile NPs are observed.

Tracking movement of the trapped NPoMs shows spatial diffusion confined to wells of <1 μm diameter with diffusivity of <0.1 $\mu m^2 s^{-1}$ (Fig. 3c), while the dark-field resonance remains constant (Fig. 3d). For hindered or confined diffusion, the mean squared displacement of the particle is no longer expected to scale linearly with observation time, and is said to be subdiffusive[36,37], empirically scaling with time to a power α as $\langle \Delta r^2 \rangle = 4\Gamma \Delta t^{\alpha}$. The diffusivity is replaced with the transport coefficient Γ, and α gives a measure of the degree to which the diffusion is anomalous, with 1 being normal diffusion and 0 fully confined (often referred to as 'compartmentalized'). Many AuNPs were tested for their subdiffusive properties and it was found that for faster-moving particles diffusion is normal ($\alpha \sim 1$), however for the confined and slower-moving particles, diffusion was found to be anomalous. For these subdiffusive particles, even at the shortest timescales the diffusion is anomalous (typical $\alpha < 0.5$), hence if the normal diffusion coefficient is taken to be 1.5 $\mu m^2 s^{-1}$, the 'compartment' sizes must be typically smaller than $\sim$1 μm (extraction of anomalous exponents, characteristic times and length-scales is detailed in Supporting Information, with examples in Fig. S9). This agrees with our other observations.

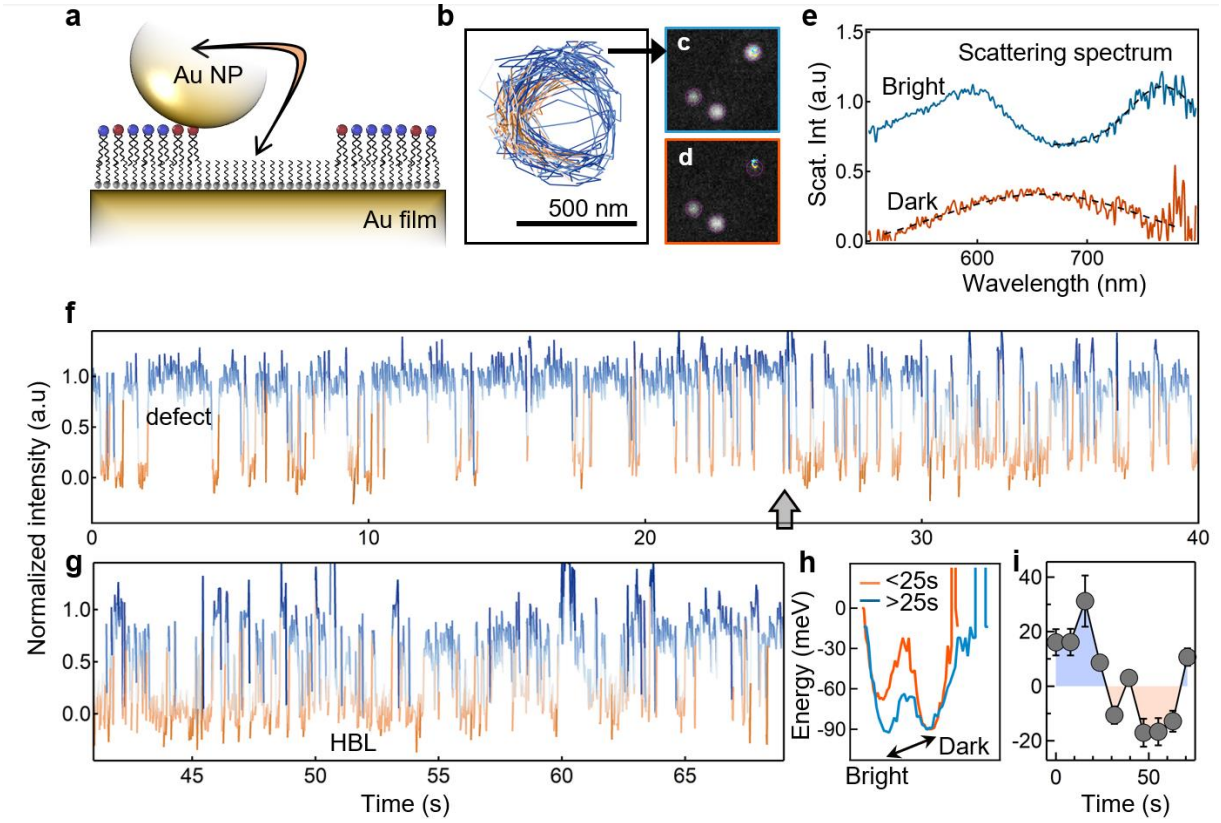

Figure 4. Dynamics of bistable AuNP on HBL. (a) Schematic motion of AuNPs that exhibit bistable confinement. (b) Particle track for one such confined AuNP and (c,d) dark-field images showing this particle (upper right), classed into two distinct intensity states (red, blue). (e) Dark-field spectra for these two states, showing different intensity and resonant peak positions. (f,g) Time trace of dark-field intensity for this particle showing binary switching behavior. After 25 s, the particle switches to being more likely found in the dark state. (h) Energy potential of bright and dark states estimated from intensity fluctuations before and after 25 s. (i) Equilibrium energies extracted from the bright/dark transition rates.

In rare instances we observe nanoparticles in a bistable state, trapped at the boundary between bilayers and defects, resulting in the NP fluctuating between being in and out of the defects (schematic in Fig. 4a). Such NPs are identified as blinking nanoparticles in the darkfield video (frames in Fig. 4c,d; full video in Supporting Information). Dark-field spectra of the nanoparticle in the dark state show a resonance at 650 nm corresponding to the larger gap size of the full HBL. However, the resonance at 750 nm in the bright state corresponds to the gap within defects (of the bare ODT monolayer). Tracking this intensity over 30 s reveals the local 3D morphology of the HBL (Fig. 4b). The assembly of lipids around the HBL edge is not static; there is a clear change in statistics of flipping dynamics after 25 s. Initially the nanoparticle is more stable on the HBL, whereas after 25 s the nanoparticle appears to spend more time in the defect (Fig. 4f,g), indicating dynamic reassembly of lipids in the raft at the base of the nanoparticle.

Comparing the intensity histogram before and after t=25 s indicates that the probability of the NP being on the bilayer (dark state) has not changed but the surface energy on the defect (bright state) is modified as the NP explores the surface.

To further quantify this flipping rate, intensity traces are classed into dark/bright states (Supporting Information, Fig. S7a) and the rate of flipping on and off the HBL is estimated. This allows us to extract the trapping energy $U(r) = -k_{\mathrm{B}}T\ln(k_{\mathrm{on}}/k_{\mathrm{off}})$, with k_{B} the Boltzmann constant, and T the bath temperature. From these estimated energies (Fig. 4i and Fig. S7b) the NP is more stable in the defect during the first 20 s, and later the equilibrium shifts to the HBL. The estimated equilibrium energies are <20 meV allowing the thermal bath to drive these modifications. The tethering of the NP to this edge could be due to the interplay of interactions with cationic DOTAP lipids and with the defect, which would explain why the NP never enters the central region of the defect. We note that the local heating caused by the enhanced optical absorption of AuNPs has negligible effects and does not alter the diffusion of NPoMs or the local refractive index. The temperature of AuNPs measured via the anti-Stokes Raman scattering match the ambient room temperature, within the experimental error (Fig. S10). Additionally, the diffusivities of mobile NPoMs remain unchanged at different dark-field white light intensities (Fig. S11). This concludes that optical absorption of NPoMs has negligible effects on the diffusion dynamics measured here.

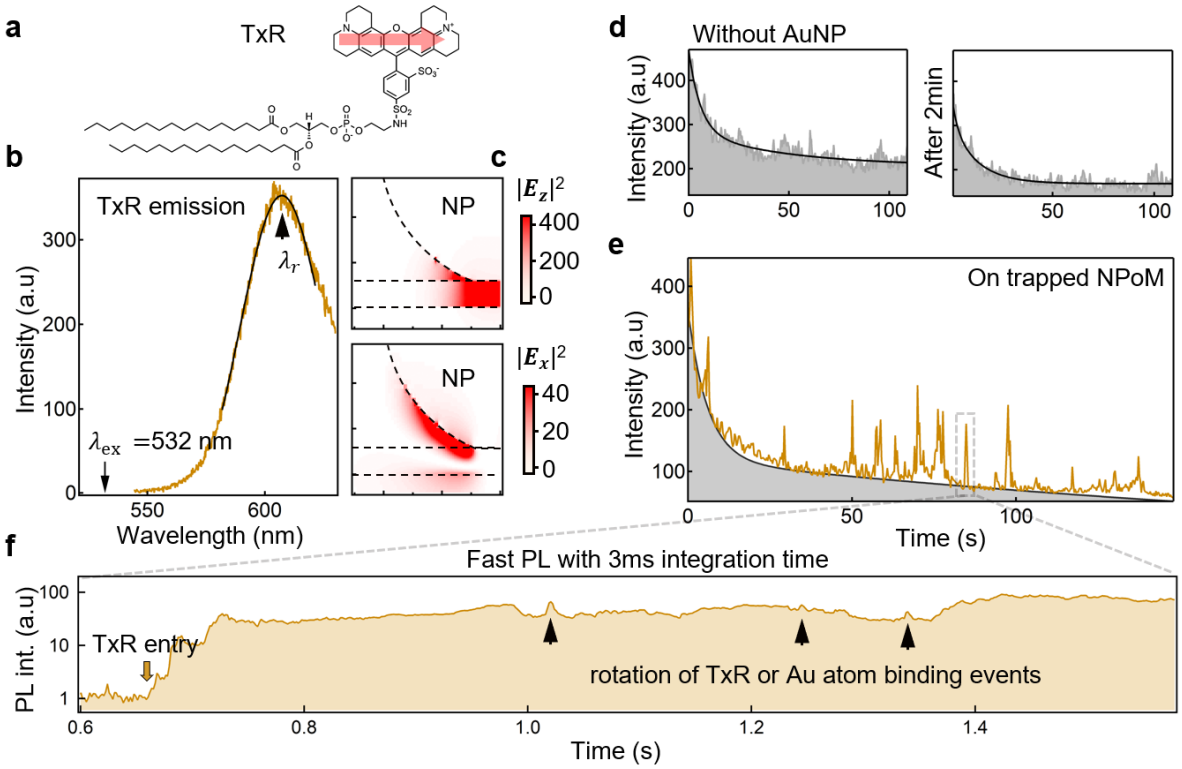

Figure 5. Dye dynamics in HBL near AuNP. (a) Chemical structure of Texas Red (TxR)-labelled lipid molecule used to dope the HBL at 0.5% molar ratio. Transition dipole orientation of TxR indicated with red arrow. (b) Fluorescence emission from TxR in HBL inside NPoM gaps, excited by 532 nm laser. (c) Near-field intensity enhancement around NPoM calculated at λ_r for E_z (top) and E_x (bottom) field components. (d) Monitored intensity of TxR away from NPoM, exhibiting bleaching dynamics fitted with double exponential (black curve). Intensity from the same area partially recovers when the laser is switched off for 2 min and then on again (right). Integration time is 50 ms. (e) Similar time-series experiment on NPoM showing short bursts of fluorescence along with slow bleaching, indicating diffusion of single TxR molecules in/out of NPoM gap. (f) Fluorescence intensity trace acquired at fast scan rates for integration times of 3 ms, capturing the dynamics of single TxR lipid molecule entering the NPoM cavity and its interaction with the metal surface.

To further explore this diffusion and reorganization of lipids around trapped NPoMs, a small fraction (0.5% molar ratio) of lipid molecules tagged with the fluorescent dye Texas Red (TxR, Fig. 5a) was introduced. The TxR-doped HBL is excited with a 532 nm laser (where TxR strongly absorbs, Supporting Information) and emission from the same diffraction-limited spot is collected by the same objective, filtered from the excitation light, and focused into a spectrometer. Fluorescence fluctuations arising from the diffusion of TxR in the bilayers is recorded for at least 100 s. If the HBL is irradiated away from any NPoM, weak emission from TxR is observed and the intensity bleaches over time (Fig. 5d). Partial recovery of photo-bleached

intensity is observed on the same area after 2 min, confirming the diffusive nature of the upper leaflet of the HBL even after labeling with TxR.

Fluorescence emission from the NPoM exhibits a completely different behavior (Fig. 5e), with strong bursts of fluorescence superimposed on the PL from surrounding HBL regions which slowly bleaches. These intense bursts represent diffusion of single TxR molecules into the plasmonic nanogaps. The light is strongly confined inside the NPoM gaps, and the emission is therefore resonantly enhanced by the Purcell factor, which exceeds 1000 for a molecule with vertical dipole orientation placed at the center of the nanogap, compared to molecules in free space[29]. The change in PL intensity is strongly correlated with changes in peak of emission wavelength and width of the PL spectra (Fig. S6). As TxR molecules diffuse within the upper leaflet of the HBL around the edge of the defects, they emit strong fluorescence while entering the enhanced optical field near the NPoM. Within the diffraction limited focal area $\sim$1 μm^2, the number of TxR molecules expected is $\sim$1.5 x 10^4. Within the NPoM cavity mode area ($\sim$125 nm^2) there would be around 1 TxR molecule (1 TxRed per 130 nm^2). This factor $\sim 10^4$ between the two is approximately the same as the enhancement factor, explaining why the emission spikes are similar in magnitude to that of the initial background fluorescence before photobleaching.

The intensity of emission is strongly influenced by the orientation of the TxR molecule in the optical fields around the NPoM. Since the TxR is covalently bound to the lipid head group, the transition dipole aligns mostly in-plane ($E_{x,y}$) with the weaker out-of-plane component (E_z) only arising due to the bending and flexing of lipids. The NPoM structure however supports stronger E_z fields (Fig. 5c) which can potentially enhance TxR emission by 500 times. Since these highest fields are confined inside the narrow gaps, it is not clear if they are fully accessible to the TxR, but the fluctuations within each 'burst' appear to correspond to the flexing motion of the lipids. In contrast, the E_x fields around the edge of the NPoM gap are easily accessed by the diffusing TxR and this results in the strong bursts of fluorescence observed. For a 100 nm AuNP, the typical time for a freely diffusing lipid (or TxR) molecule to traverse the nanoparticle is $\sim$2.5 ms, and considerably less time to traverse the plasmonic cavity. To resolve this we record fast PL with 3 ms resolution, which shows slow diffusion of single TxR lipids into the cavity (Fig. 5f, note $\log(\mathrm{PL})$ scale). As the TxR enters the cavity the overall PL intensity increases by an average of 100 times (so the PL of single TxR is enhanced by $\sim 10^6$), but the PL intensity still exhibits strong fluctuations associated with rotational diffusion of the TxR. The recruitment of DOTAP molecules in the lipid layer, creating a raft under the AuNP, is likely to cause a significant reduction of TxR diffusion rates in and around the cavity as we observe.

The HBLs are supported on a solid surface and consist of a single mobile layer of lipid molecules (the other layer being the immobile thiol SAM). This is likely to affect the mobility of the lipid layer and of any components embedded within the membrane (typical lipid diffusivity in a

supported bilayer is ~3 $\mu m^2 s^{-1}$, but considerably higher in unsupported membranes such as in giant unilamellar vesicles[38]). Viscous drag will affect the mobility of the upper lipid layer, and surface interactions make it challenging to introduce full transmembrane proteins into this system. We thus anticipate further development to include 'unsupported' lipid membranes with AuNP attachment on both sides, removing the complications of substrate interactions. The HBL model does however still capture many of the properties of a cell membrane, including most importantly, lateral fluidity of the lipid layer.

This work provides insight into the nanoscopic organization of lipid bilayers and their defects around gold nanoparticles. The corresponding motion of these AuNPs together with their spectroscopic information, provides dynamic topographical information. We observe instances where NPs diffuse as freely as lipid molecules in the membrane whilst being electrostatically attached to the DOTAP molecules present. We also see cases where NPs sit inside defects in the bilayer and reorganize lipids around them, exhibiting confined diffusion. The latter case shows significant activity in darkfield spectra with the resonance peak shifts tracking fluctuations in *z*-height. Most importantly, we note that the NPs do not appear to perturb the lipid membrane structure other than possible recruitment of charged components in the vicinity of pre-existing defects. From this, we conclude that the HBL system used with the NPoM geometry is well suited to study out-of-plane motion of lipids and diffusion associated with the membrane. Alternative models may be required if large and complex moieties that span the membrane, such as proteins are to be studied.

METHODS: Template Stripped Gold. A silicon wafer is cleaned using a 10% Decon 90 solution, and rinsed twice with water, ethanol and isopropanol. A 100 nm thick layer of gold is evaporated on the wafer at 1 $Å s^{-1}$ using a Kurt J. Lesker E-beam evaporator. The Au coated silicon wafer was heated to 60°C and smaller pieces of silicon wafer were glued to the surface using an Epo-Tek 377 epoxy glue, which was cured at 150°C for 18 hours. The wafer was then allowed to gradually cool to room temperature and individual pieces of silicon were peeled off, exposing a flat and clean gold surface, prior to functionalization with octadecanethiol.

Hybrid Lipid Bilayer Preparation. Template stripped gold was incubated overnight at room temperature in ethanol containing 5 mM octadecanethiol (ODT) (Sigma), forming a self-assembled monolayer (SAM). After monolayer deposition the substrates were rinsed thoroughly with ethanol, dried under a stream of nitrogen and used immediately. 1 mg of dried palmitoyl-oleoyl phosphatidylcholine (Avanti Polar Lipids, Alabaster, AL) was re-suspended by vortexing in 1 mL phosphate buffered saline (PBS) solution (Sigma) and extruded 21 times through a 50 nm track etch membrane (Whatman) using a mini extruder kit (Avanti Polar Lipids). The resulting suspension turned clear to indicate the formation of small unilamellar vesicles, which were stored in the fridge and used within a few days. When ready for use, the vesicle suspension was diluted in PBS to a concentration of 0.5 mg/mL, and injected into a custom-built flow-cell which

contained a piece of template stripped gold with an ODT SAM, and incubated for 60 minutes. The sample was then rinsed with MilliQ water, and subsequently more PBS.

Dark-field Microscopy. The final step to prepare the sample for imaging was to inject 100 nm gold nanoparticles into the flow-cell. These were incubated for approximately 1 min before the excess was carefully rinsed away with PBS. The flow-cell was then placed on the microscope stage under a darkfield 100× (0.8NA) objective for imaging (optical setup, Fig. S1 in Supporting Information). The darkfield video are recorded in monochromatic mode with 50 ms for each frame and with refresh time of 70 ms between each frame. The darkfield Spectra were recorded from a wide area of 5 × 5 μm at a rate of 2 Hz, using a QE65000 Ocean Optics spectrometer, whilst being illuminated with a halogen lamp.

Single Particle Tracking. Videos of diffusing AuNPs were processed in FIJI software, and the AuNPs were identified and tracked using the single particle tracking plugin TrackMate[39]. This yielded a collection of particle tracks which represented the motion of each of the AuNPs in the video together with their intensity values at each point in time. This information was subsequently used to obtain diffusion information including diffusivity and the anomalous exponent to help identify whether the AuNPs were undergoing free or hindered diffusion.

Atomic Force Microscopy. Atomic force microscopy (AFM) measurements were performed in fluid conditions at room temperature in tapping mode using a Dimension FastScan Bio with Fast Scan D probes (Bruker), short cantilevers with a spring constant of ~0.25 Nm^{-1} and a resonance frequency of 110 kHz. The force applied by the tip on the sample was minimized by maximizing the set point whilst maintaining tracking of the surface.

ASSOCIATED CONTENT

Supporting Information. Dark-field videos showing the diffusion of AuNPs on the HBL are available online. A Supporting Information document is also provided, with additional images and information.

AUTHOR INFORMATION

Corresponding Author

* Dr Rohit Chikkaraddy, rc621@cam.ac.uk
* Prof Jeremy J Baumberg, jjb12@cam.ac.uk

ORCID

Rohit Chikkaraddy: 0000-0002-3840-4188
Jeremy J Baumberg: 0000-0002-9606-9488

Notes

The authors declare no competing financial interest.

ACKNOWLEDGMENT

We acknowledge support from EPSRC grants EP/G060649/1, EP/L027151/1, EP/G037221/1, and EPSRC NanoDTC. R.C. acknowledges support from Trinity College, University of Cambridge. B.d.N acknowledges support from the Leverhulme Trust and Isaac Newton Trust in the form of an Early Career Fellowship.

REFERENCES

(1) Arroyo, J. O.; Kukura, P. Non-Fluorescent Schemes for Single-Molecule Detection, Imaging and Spectroscopy. *Nat. Photonics* **2016**, *10* (1), 11–17. https://doi.org/10.1038/nphoton.2015.251.

(2) Limaj, O.; Etezadi, D.; Wittenberg, N. J.; Rodrigo, D.; Yoo, D.; Oh, S.-H.; Altug, H. Infrared Plasmonic Biosensor for Real-Time and Label-Free Monitoring of Lipid Membranes. *Nano Lett.* **2016**, *16* (2), 1502–1508. https://doi.org/10.1021/acs.nanolett.5b05316.

(3) Guo, Y.; Terazzi, E.; Seemann, R.; Fleury, J. B.; Baulin, V. A. Direct Proof of Spontaneous Translocation of Lipid-Covered Hydrophobic Nanoparticles through a Phospholipid Bilayer. *Sci. Adv.* **2016**, *2* (11), e1600261. https://doi.org/10.1126/sciadv.1600261.

(4) Li, Y.; Lin, T.; Luo, Y.; Liu, Q.; Xiao, W.; Guo, W.; Lac, D.; Zhang, H.; Feng, C.; Wachsmann-Hogiu, S.; et al. A Smart and Versatile Theranostic Nanomedicine Platform Based on Nanoporphyrin. *Nat. Commun.* **2014**, *5*, 4712. https://doi.org/10.1038/ncomms5712.

(5) Lin, J.; Zhang, H.; Chen, Z.; Zheng, Y. Penetration of Lipid Membranes by Gold Nanoparticles: Insights into Cellular Uptake, Cytotoxicity, and Their Relationship. *ACS Nano* **2010**, *4* (9), 5421–5429. https://doi.org/10.1021/nn1010792.

(6) Johnston, H. J.; Hutchison, G.; Christensen, F. M.; Peters, S.; Hankin, S.; Stone, V. A Review of the in Vivo and in Vitro Toxicity of Silver and Gold Particulates: Particle Attributes and Biological Mechanisms Responsible for the Observed Toxicity. *Crit. Rev. Toxicol.* **2010**, *40* (4), 328–346. https://doi.org/10.3109/10408440903453074.

(7) Zimmerman, J. F.; Ardoña, H. A. M.; Pyrgiotakis, G.; Dong, J.; Moudgil, B.; Demokritou, P.; Parker, K. K. Scatter Enhanced Phase Contrast Microscopy for Discriminating Mechanisms of Active Nanoparticle Transport in Living Cells. *Nano Lett.* **2019**, *19* (2), 793–804. https://doi.org/10.1021/acs.nanolett.8b03903.

(8) Lesniak, A.; Fenaroli, F.; Monopoli, M. P.; Åberg, C.; Dawson, K. A.; Salvati, A. Effects of the Presence or Absence of a Protein Corona on Silica Nanoparticle Uptake and Impact on Cells. *ACS Nano* **2012**, *6* (7), 5845–5857. https://doi.org/10.1021/nn300223w.

(9) Chithrani, B. D.; Chan, W. C. W. Elucidating the Mechanism of Cellular Uptake and Removal of Protein-Coated Gold Nanoparticles of Different Sizes and Shapes. *Nano Lett.* **2007**, *7* (6), 1542–1550. https://doi.org/10.1021/nl070363y.

(10) Singer, S. J.; Nicolson, G. L. The Fluid Mosaic Model of the Structure of Cell Membranes. *Science* **1972**, *175* (4023), 720–731. https://doi.org/10.1126/science.175.4023.720.
(11) Ritchie, K.; Iino, R.; Fujiwara, T.; Murase, K.; Kusumi, A. The Fence and Picket Structure of the Plasma Membrane of Live Cells as Revealed by Single Molecule Techniques (Review). *Mol. Membr. Biol.* **2003**, *20* (1), 13–18. https://doi.org/10.1080/0968768021000055698.
(12) Tarun, O. B.; Hannesschläger, C.; Pohl, P.; Roke, S. Label-Free and Charge-Sensitive Dynamic Imaging of Lipid Membrane Hydration on Millisecond Time Scales. *Proc. Natl. Acad. Sci.* **2018**, *115* (16), 4081–4086. https://doi.org/10.1073/pnas.1719347115.
(13) Coker, H. L. E.; Cheetham, M. R.; Kattnig, D. R.; Wang, Y. J.; Garcia-Manyes, S.; Wallace, M. I. Controlling Anomalous Diffusion in Lipid Membranes. *Biophys. J.* **2019**, *116* (6), 1085–1094. https://doi.org/10.1016/j.bpj.2018.12.024.
(14) Chee, S. W.; Anand, U.; Bisht, G.; Tan, S. F.; Mirsaidov, U. Direct Observations of the Rotation and Translation of Anisotropic Nanoparticles Adsorbed at a Liquid–Solid Interface. *Nano Lett.* **2019**, *19* (5), 2871–2878. https://doi.org/10.1021/acs.nanolett.8b04962.
(15) Fu, X.; Chen, B.; Tang, J.; Hassan, M. T.; Zewail, A. H. Imaging Rotational Dynamics of Nanoparticles in Liquid by 4D Electron Microscopy. *Science* **2017**, *355* (6324), 494–498. https://doi.org/10.1126/science.aah3582.
(16) Regmi, R.; Winkler, P. M.; Flauraud, V.; Borgman, K. J. E.; Manzo, C.; Brugger, J.; Rigneault, H.; Wenger, J.; García-Parajo, M. F. Planar Optical Nanoantennas Resolve Cholesterol-Dependent Nanoscale Heterogeneities in the Plasma Membrane of Living Cells. *Nano Lett.* **2017**, *17* (10), 6295–6302. https://doi.org/10.1021/acs.nanolett.7b02973.
(17) Winkler, P. M.; Regmi, R.; Flauraud, V.; Brugger, J.; Rigneault, H.; Wenger, J.; García-Parajo, M. F. Optical Antenna-Based Fluorescence Correlation Spectroscopy to Probe the Nanoscale Dynamics of Biological Membranes. *J. Phys. Chem. Lett.* **2018**, *9* (1), 110–119. https://doi.org/10.1021/acs.jpclett.7b02818.
(18) Winkler, P. M.; Regmi, R.; Flauraud, V.; Brugger, J.; Rigneault, H.; Wenger, J.; García-Parajo, M. F. Transient Nanoscopic Phase Separation in Biological Lipid Membranes Resolved by Planar Plasmonic Antennas. *ACS Nano* **2017**, *11* (7), 7241–7250. https://doi.org/10.1021/acsnano.7b03177.
(19) Taylor, R. W.; Mahmoodabadi, R. G.; Rauschenberger, V.; Giessl, A.; Schambony, A.; Sandoghdar, V. Interferometric Scattering Microscopy Reveals Microsecond Nanoscopic Protein Motion on a Live Cell Membrane. *Nat. Photonics* **2019**, *13* (7), 480–487. https://doi.org/10.1038/s41566-019-0414-6.
(20) Taylor, R. W.; Sandoghdar, V. Interferometric Scattering Microscopy: Seeing Single Nanoparticles and Molecules via Rayleigh Scattering. *Nano Lett.* **2019**, *19* (8), 4827–4835. https://doi.org/10.1021/acs.nanolett.9b01822.
(21) Wit, G. de; Danial, J. S. H.; Kukura, P.; Wallace, M. I. Dynamic Label-Free Imaging of Lipid Nanodomains. *Proc. Natl. Acad. Sci.* **2015**, *112* (40), 12299–12303. https://doi.org/10.1073/pnas.1508483112.
(22) de Wit, G.; Albrecht, D.; Ewers, H.; Kukura, P. Revealing Compartmentalized Diffusion in Living Cells with Interferometric Scattering Microscopy. *Biophys. J.* **2018**, *114* (12), 2945–2950. https://doi.org/10.1016/j.bpj.2018.05.007.

(23) Brolo, A. G. Plasmonics for Future Biosensors. *Nat. Photonics* **2012**, *6*, 709–713. https://doi.org/10.1038/nphoton.2012.266.
(24) Baumberg, J. J.; Aizpurua, J.; Mikkelsen, M. H.; Smith, D. R. Extreme Nanophotonics from Ultrathin Metallic Gaps. *Nat. Mater.* **2019**, 1. https://doi.org/10.1038/s41563-019-0290-y.
(25) Baaske, M. D.; Foreman, M. R.; Vollmer, F. Single-Molecule Nucleic Acid Interactions Monitored on a Label-Free Microcavity Biosensor Platform. *Nat. Nanotechnol.* **2014**, *9* (11), 933–939. https://doi.org/10.1038/nnano.2014.180.
(26) Lum, W.; Bruzas, I.; Gorunmez, Z.; Unser, S.; Beck, T.; Sagle, L. Novel Liposome-Based Surface-Enhanced Raman Spectroscopy (SERS) Substrate. *J. Phys. Chem. Lett.* **2017**, *8* (12), 2639–2646. https://doi.org/10.1021/acs.jpclett.7b00694.
(27) Taylor, R. W.; Benz, F.; Sigle, D. O.; Bowman, R. W.; Bao, P.; Roth, J. S.; Heath, G. R.; Evans, S. D.; Baumberg, J. J. Watching Individual Molecules Flex within Lipid Membranes Using SERS. *Sci. Rep.* **2014**, *4*, 5940. https://doi.org/10.1038/srep05940.
(28) Kongsuwan, N.; Demetriadou, A.; Chikkaraddy, R.; Benz, F.; Turek, V. A.; Keyser, U. F.; Baumberg, J. J.; Hess, O. Suppressed Quenching and Strong-Coupling of Purcell-Enhanced Single-Molecule Emission in Plasmonic Nanocavities. *ACS Photonics* **2018**, *5* (1), 186–191. https://doi.org/10.1021/acsphotonics.7b00668.
(29) Chikkaraddy, R.; Turek, V. A.; Kongsuwan, N.; Benz, F.; Carnegie, C.; van de Goor, T.; de Nijs, B.; Demetriadou, A.; Hess, O.; Keyser, U. F.; et al. Mapping Nanoscale Hotspots with Single-Molecule Emitters Assembled into Plasmonic Nanocavities Using DNA Origami. *Nano Lett.* **2018**, *18* (1), 405–411. https://doi.org/10.1021/acs.nanolett.7b04283.
(30) Chikkaraddy, R.; Zheng, X.; Benz, F.; Brooks, L. J.; de Nijs, B.; Carnegie, C.; Kleemann, M.-E.; Mertens, J.; Bowman, R. W.; Vandenbosch, G. A. E.; et al. How Ultranarrow Gap Symmetries Control Plasmonic Nanocavity Modes: From Cubes to Spheres in the Nanoparticle-on-Mirror. *ACS Photonics* **2017**, *4* (3), 469–475. https://doi.org/10.1021/acsphotonics.6b00908.
(31) Nijs, B. de; Bowman, R. W.; Herrmann, L. O.; Benz, F.; Barrow, S. J.; Mertens, J.; Sigle, D. O.; Chikkaraddy, R.; Eiden, A.; Ferrari, A.; et al. Unfolding the Contents of Sub-Nm Plasmonic Gaps Using Normalising Plasmon Resonance Spectroscopy. *Faraday Discuss.* **2015**, *178* (0), 185–193. https://doi.org/10.1039/C4FD00195H.
(32) Kleemann, M.-E.; Mertens, J.; Zheng, X.; Cormier, S.; Turek, V.; Benz, F.; Chikkaraddy, R.; Deacon, W.; Lombardi, A.; Moshchalkov, V. V.; et al. Revealing Nanostructures through Plasmon Polarimetry. *ACS Nano* **2017**, *11* (1), 850–855. https://doi.org/10.1021/acsnano.6b07350.
(33) Fujiwara, T.; Ritchie, K.; Murakoshi, H.; Jacobson, K.; Kusumi, A. Phospholipids Undergo Hop Diffusion in Compartmentalized Cell Membrane. *J. Cell Biol.* **2002**, *157* (6), 1071–1082. https://doi.org/10.1083/jcb.200202050.
(34) Lee, Y. K.; Kim, S.; Oh, J.-W.; Nam, J.-M. Massively Parallel and Highly Quantitative Single-Particle Analysis on Interactions between Nanoparticles on Supported Lipid Bilayer. *J. Am. Chem. Soc.* **2014**, *136* (10), 4081–4088. https://doi.org/10.1021/ja501225p.
(35) Liao, Y.-H.; Lin, C.-H.; Cheng, C.-Y.; Wong, W. C.; Juo, J.-Y.; Hsieh, C.-L. Monovalent and Oriented Labeling of Gold Nanoprobes for the High-Resolution Tracking of a Single-Membrane Molecule. *ACS Nano* **2019**. https://doi.org/10.1021/acsnano.9b01176.

(36) Saxton, M. J. A Biological Interpretation of Transient Anomalous Subdiffusion. II. Reaction Kinetics. *Biophys. J.* **2008**, *94* (3), 760–771. https://doi.org/10.1529/biophysj.107.114074.
(37) Murase, K.; Fujiwara, T.; Umemura, Y.; Suzuki, K.; Iino, R.; Yamashita, H.; Saito, M.; Murakoshi, H.; Ritchie, K.; Kusumi, A. Ultrafine Membrane Compartments for Molecular Diffusion as Revealed by Single Molecule Techniques. *Biophys. J.* **2004**, *86* (6), 4075–4093. https://doi.org/10.1529/biophysj.103.035717.
(38) Przybylo, M.; Sýkora, J.; Humpolíčková, J.; Benda, A.; Zan, A.; Hof, M. Lipid Diffusion in Giant Unilamellar Vesicles Is More than 2 Times Faster than in Supported Phospholipid Bilayers under Identical Conditions. *Langmuir* **2006**, *22* (22), 9096–9099. https://doi.org/10.1021/la061934p.
(39) Tinevez, J.-Y.; Perry, N.; Schindelin, J.; Hoopes, G. M.; Reynolds, G. D.; Laplantine, E.; Bednarek, S. Y.; Shorte, S. L.; Eliceiri, K. W. TrackMate: An Open and Extensible Platform for Single-Particle Tracking. *Methods* **2017**, *115*, 80–90. https://doi.org/10.1016/j.ymeth.2016.09.016.